Shallow and Deep Latent Heating Modes over Tropical Oceans Observed with TRMM PR Spectral Latent Heating Data

YUKARI N. TAKAYABU

Center for Climate System Research, The University of Tokyo, Chiba, Japan

SHOICHI SHIGE*

Osaka Prefecture University, Osaka, Japan

WEI-KUO TAO

NASA Goddard Space Flight Center, Greenbelt, Maryland

NAGIO HIROTA

Center for Climate System Research, The University of Tokyo, Chiba, Japan

(Manuscript received 3 March 2009, in final form 19 September 2009)

ABSTRACT

Three-dimensional distributions of the apparent heat source (Q_1) − radiative heating (Q_R) estimated from Tropical Rainfall Measuring Mission (TRMM) Precipitation Radar (PR) utilizing the spectral latent heating (SLH) algorithm are analyzed. Mass-weighted and vertically integrated $Q_1 - Q_R$ averaged over the tropical oceans is estimated as ~72.6 J s^{-1} (~2.51 mm day^{-1}) and that over tropical land is ~73.7 J s^{-1} (~2.55 mm day^{-1}) for 30°N–30°S. It is shown that nondrizzle precipitation over tropical and subtropical oceans consists of two dominant modes of rainfall systems: deep systems and congestus. A rough estimate of the shallow-heating contribution against the total heating is about 46.7% for the average tropical oceans, which is substantially larger than the 23.7% over tropical land.

Although cumulus congestus heating linearly correlates with SST, deep-mode heating is dynamically bounded by large-scale subsidence. It is notable that a substantial amount of rain, as large as 2.38 mm day^{-1} on average, is brought from congestus clouds under the large-scale subsiding circulation. It is also notable that, even in the region with SSTs warmer than 28°C, large-scale subsidence effectively suppresses the deep convection, with the remaining heating by congestus clouds.

The results support that the entrainment of mid–lower-tropospheric dry air, which accompanies the large-scale subsidence, is the major factor suppressing the deep convection. Therefore, a representation of the realistic entrainment is very important for proper reproduction of precipitation distribution and the resultant large-scale circulation.

1. Introduction

Over the tropical and subtropical oceans, destabilization of the atmosphere by warm sea surface temperatures (SSTs) and the stabilization by subsidence and horizontal transport may be compared. As a result, although a large precipitation amount is observed with very high SSTs, it does not significantly correlate with SST over moderately warm sea surfaces. Various studies indicate that SST works as a threshold for the precipitation activity (e.g., Gadgil et al. 1984). In the current climate, 28°C may be a generally good rule of thumb as a threshold for deep convection; however, the circulation is probably more important in determining the value of the threshold.

* Current affiliation: Graduate School of Science, Kyoto University, Kyoto, Japan.

Corresponding author address: Yukari N. Takayabu, Center for Climate System Research, The University of Tokyo, 5-1-5 Kashiwanoha, Kashiwa, Chiba, 277-8568, Japan.
E-mail: yukari@ccsr.u-tokyo.ac.jp

Under the influence of large-scale subsidence, a resulting temperature inversion and dry layer in the mid–low troposphere are two factors suppressing deep convection. Historically, tropical convective clouds were considered to have a "bimodal structure," consisting of deep cumulus convection and shallow trade inversion cumuli. In the 1990s, a melting level stable layer and associated prominence of cumulus congestus clouds were reported over the western Pacific warm pool region from the Tropical Ocean Global Atmosphere Coupled Ocean–Atmosphere Response Experiment (TOGA COARE) (Johnson et al. 1999). Since then, our understanding of the tropical convection has expanded from bimodal to trimodal structures—that is, deep convection, cumulus congestus, and shallow cumuli.

Substantial contribution of cumulus congestus is also reported by Petty (1999), utilizing surface synoptic reports together with infrared images of the Japanese fifth geostationary meteorological satellite (*GMS-5*). He concluded that a substantial fraction (20%–40%) of precipitation comes from clouds warmer than 273 K in a large area to the east of Australia. Mapes (2000) also emphasized the significant role of cumulus congestus in helping to balance between the convective heating and atmospheric radiative cooling. Short and Nakamura (2000) utilized the Tropical Rainfall Measuring Mission (TRMM) Precipitation Radar (PR) data and estimated the precipitation associated with shallow rain accounts for ~20% of total tropical precipitation. More recently, Kubar and Hartmann (2008) utilized CloudSat data to compare the vertical structure of cloud systems of the intertropical convergence zone (ITCZ) across the east and west Pacific. They found that, associated with moderate intensity rainfall and also with mid-level thick systems, two peaks in the cloud-top distribution at ~6 and ~2 km are significant. The trimodal structure is also observed in association with a three-step-wise development of large-scale cloud systems such as the Madden–Julian oscillation (MJO) over the western Pacific (Kikuchi and Takayabu 2004).

The importance of a substantial amount of shallow heating is emphasized by Zhang et al. (2004), who found a low-level meridional return flow associated with the shallow heating in the eastern Pacific ITCZ. Wu (2003) investigated the circulation driven by deep heating and shallow congestus heating by linear equations and a dry primitive equation model, and he showed that low-level moisture convergence driven by shallow congestus heating is 5 times larger than the deep heating of the same amount and exceeds the value to maintain the heat source. On the other hand, moisture convergence associated with deep heating is not efficient enough to sustain the heating. He estimated about 24% of the total precipitation must be associated with shallow heating.

In the atmospheric general circulation models (AGCMs), tropical cumulus convection is dealt with by various cumulus parameterizations, which represent effects of the subgrid-scale cumulus convection with grid-scale variables; however, it has been noticed that many AGCMs produce an incorrect distribution of tropical precipitation. One of the frequently reported problems is the unrealistically parallel distribution of the intertropical convergence zones in both hemispheres along the equator (double ITCZ). Also, Bony and Dufrence (2005) reported that the largest disagreements in sensitivity of cloud radiative forcing (CRF) among climate models and between models and observations are found in regions of large-scale subsidence. Their study indicates that at least some of the cumulus parameterizations utilized in AGCMs do not properly represent the suppression of deep convection under the large-scale subsidence. These results strongly suggest that understanding the mechanism of convection suppression by large-scale subsidence is essential for improvements of cumulus parameterizations.

As for the effects of environmental factors, Jensen and DelGenio (2006) utilized observations from an Atmospheric Radiation Measurement (ARM) surface-based remote sensing site at Nauru Island and indicated that a drying of the midtroposphere is more effective to limit congestus cloud-top heights compared to a freezing level–induced stable layer. This result is consistent with results of Brown and Zhang (1997), Redelsperger et al. (2002), Takemi et al. (2004), and Takayabu et al. (2006).

In this study, we analyze the three-dimensional distributions of $Q_1 - Q_R$ obtained from the spectral latent heating (SLH) data, where Q_1 is the apparent heat source invented by Yanai et al. (1973) and Q_R is the radiative heating. Utilizing field campaign soundings, Schumacher et al. (2007, 2008) presented total diabatic heating profiles that represent the dominant cloud types. The first purpose of this study is to quantitatively examine $Q_1 - Q_R$ distributions over the global tropical oceans. We find two predominant $Q_1 - Q_R$ modes, a deep mode and a shallow mode, associated with nondrizzle precipitation. Next, we aim to find the controlling environmental factors of these two vertical modes of precipitation systems. Note that this bimodal structure is not the same as the well-documented two primary modes; rather, it corresponds to the upper two modes of the trimodal structure found by Johnson et al. (1999): deep convection and cumulus congestus. The TRMM PR rarely detects weak precipitation associated with trade cumuli because of its reflectivity sensitivity of 17 dBZ; therefore, we cannot quantify the contribution of trade cumuli in this study. It is assumed here that such a light rain contribution from trade cumuli does not largely increase the shallow rain
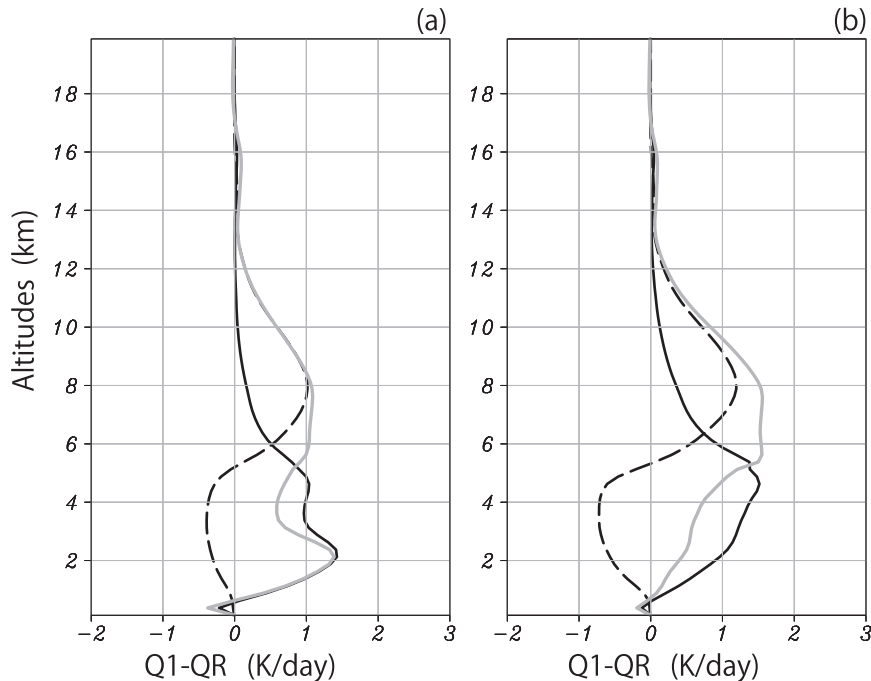
FIG. 1. Eight-year unconditional mean $Q_1 - Q_R$ profiles averaged for 30°N–30°S at all longitudes (a) over the ocean and (b) over land. Black solid lines indicate $Q_1 - Q_R$ associated with convective rain, black-dashed lines indicate $Q_1 - Q_R$ with stratiform rain, and gray solid lines are those associated with total rain.

contribution, which should be examined with recent spaceborne cloud radar observation from CloudSat in future studies.

In section 2, we describe the data utilized in this study. In section 3, the relationship between the heating distribution and the sea surface temperature is examined. In section 4, effects of large-scale subsidence on precipitation heating are examined. Finally, section 5 is devoted to summary and discussion.

2. Data and methodology

Since the launch of the TRMM satellite in December 1997, it has continuously provided a unique dataset of spaceborne precipitation radar, which has a 13.8-GHz Ku-band frequency. In this study, using the TRMM PR data and conversion tables between precipitation and latent heating, we utilized $Q_1 - Q_R$ [Eq. (1)] as a large-scale diabatic heating rate obtained from the SLH algorithm (Shige et al. 2004, 2007, 2008):

$$Q_1 \equiv \frac{D\bar{s}}{Dt} = \frac{\partial \bar{s}}{\partial t} + \bar{v} \cdot \nabla \bar{s} + \bar{\omega} \frac{\partial \bar{s}}{\partial p} = Q_R + L(\bar{c} - \bar{e})$$

$$- \nabla \cdot \overline{s'v'} - \frac{\partial}{\partial p} \overline{s'\omega'}. \quad (1)$$

Here, Q_1 is the apparent heat source invented by Yanai et al. (1973); Q_R is the radiative heating; and s is the dry

static energy, $s = C_p T + gz$. The SLH algorithm is a table method to estimate latent heating and $Q_1 - Q_R$, utilizing the TRMM PR precipitation data. Conversion tables are made from a simulation of TOGA COARE convection with the Goddard Cumulus Ensemble Model, in a spectral sense in terms of the precipitation-top height (PTH) for the convective rain and in terms of the melting level precipitation rate for the stratiform rain.

For the atmospheric variables, we utilized the Japan Meteorological Agency (JMA) Japanese 25-year Reanalysis Project (JRA25) data and the Japanese Climate Data Assimilation System (JCDAS); and for SST we used the National Oceanic and Atmospheric Administration (NOAA) optimum interpolation (OI) SST data. The analysis period is 8 yr from 1998 to 2005.

3. $Q_1 - Q_R$ versus SST

Eight-year unconditional mean $Q_1 - Q_R$ profiles averaged for 30°N–30°S at all longitudes are depicted in Fig. 1, separately for over the ocean and over land. Two peaks in the convective heating at ~5 and ~2 km are apparent over the ocean, whereas only the former peak is significant over land. When we look back to the spectral table (Shige et al. 2007), it is known that the ~5-km heating peak corresponds to deep convection, whereas the ~2-km peak is associated with the precipitation

from cumulus congestus with PTHs between 2 and 6 km. The latter may well correspond to the "moderate rain" class analyzed in Kubar and Hartmann (2008). Apparently, cumulus congestus is much more frequent over the ocean than over land. When we examine the surface rain contributions of each PTH bin for PR-based convective rain (Fig. A1 in the appendix), we notice that abundant rain from PTHs between 2 and 6 km over the ocean is missing over land; therefore, it is considered that these congestus rains contribute to the average oceanic ~2-km heating peak. Here, let us note that, because cloud-top heights associated with this type of rain may be higher than the freezing level, such cumulus congestus clouds may not purely represent warm rain processes but perhaps may include ice and/or mixed phase processes.

On the other hand, heating profiles associated with stratiform rain are characterized with positive heating in the upper troposphere with a peak at ~8 km and cooling in the lower troposphere with a peak at ~4 km, both over the ocean and over land. Deep stratiform rain comes from the nimbostratus clouds, which are associated primarily with the widespread continuous clouds of mesoscale convective systems, hurricanes, and extratropical cyclones (Houze 1993). Because rainfall contribution from the tropical cyclones in the TRMM observation region is as small as 3%–4% of the total rainfall (Yokoyama and Takayabu 2008), we can consider that this tropical stratiform heating profile mostly represents the heating of the deep stratiform rain associated with mesoscale-organized convective systems. The lower-tropospheric evaporative cooling over land is larger than that over the ocean. Total $Q_1 - Q_R$ heating profiles have a broad peak around 6–8 km over the ocean and over land and another peak at ~2 km over the ocean.

Mass-weighted and vertically integrated $Q_1 - Q_R$ averaged over the ocean from 30°N to 30°S is estimated as ~72.6 J s^{-1} (~2.51 mm day^{-1}), and that averaged over land from 30°N to 30°S is ~73.7 J s^{-1} (~2.55 mm day^{-1}). Rough estimates of the shallow-heating contribution by mass-integrated $Q_1 - Q_R$ below the freezing level of 4.5 km is about 46.7% for the average tropical oceans from 30°N to 30°S and about 23.8% for the average tropical land from 30°N to 30°S, which is still larger than values suggested by previous studies. It is interesting to note that a 46.7% shallow-heating contribution to the total heating is very similar to the contribution to total precipitation in the east Pacific ITCZ region from clouds lower than 9.5 km in the Kubar and Hartmann (2008) study.

Based on the previously mentioned heating profiles, we choose 7.5 km as a representative altitude for the upper-level heating and 2.0 km for the lower-level heating, to examine the seasonal mean horizontal distributions of upper and lower heatings (Figs. 2 and 3). The upper-level heating distributions are very similar to the total seasonal precipitation (not shown), and large values are found over very warm SSTs (>28°C) and over tropical land. However, for the moderate SST region (<28°C), the deep-heating distribution does not obediently follow the SST distribution; for example, in the southern Pacific, we find warm SST contours extend eastward nearly parallel to the equator, whereas the deep heating bends southward beyond the date line.

Much more lower-level heating is found over the ocean than over land, as shown in Fig. 3, which is consistent with what was found in Fig. 1. Second, over the ocean the heating distribution follows the SST distribution (e.g., distribution along the line from the Philippine Islands to Hawaii). It is apparent that ~2-km congestus heating exhibits more double-ITCZ-like distribution than ~7.5-km-deep heating, because the former more closely follows the SST distribution. It is interesting to note that lower-level heating is larger over the ITCZ to the east of the date line compared to the convective region over the warm pool. This is consistent with findings by Zhang et al. (2004), who emphasized the importance of shallow circulation induced by congestus heating in the eastern Pacific ITCZ region. It also agrees with a prediction of a bimodal convection model developed by Back and Bretherton (2009). Their model consists of a shallow mode, which is related to all "boundary layer convergence"; a deep mode, which is proportional to conditional instability in the surface convergence region; and realistically produced "bottom heavy" and "top heavy" contrasts of the climatological precipitation heating distribution. It is also notable that particularly large low-level and upper-level amplitudes are diagnosed along the western coasts of India and Indochina in June–August.

To further examine the SST heating relationship for deep systems and for cumulus congestus, we scattered deep heating and shallow heating against SST for each season (Figs. 4 and 5). It is clearly confirmed that SST works as a threshold for deep convective systems "to be available" at the temperature of ~27°C. On the other hand, low-level congestus heating correlates with the SST for almost the entire SST range from 18° to 30°C for every season. This confirms what we saw from the horizontal distributions in Fig. 3, suggesting that cumulus congestus activity is very obedient to the boundary layer destabilization and not especially sensitive to other large-scale factors.

4. $Q_1 - Q_R$ versus large-scale vertical velocity

Because previous studies indicate that large-scale subsidence works to suppress deep convection effectively
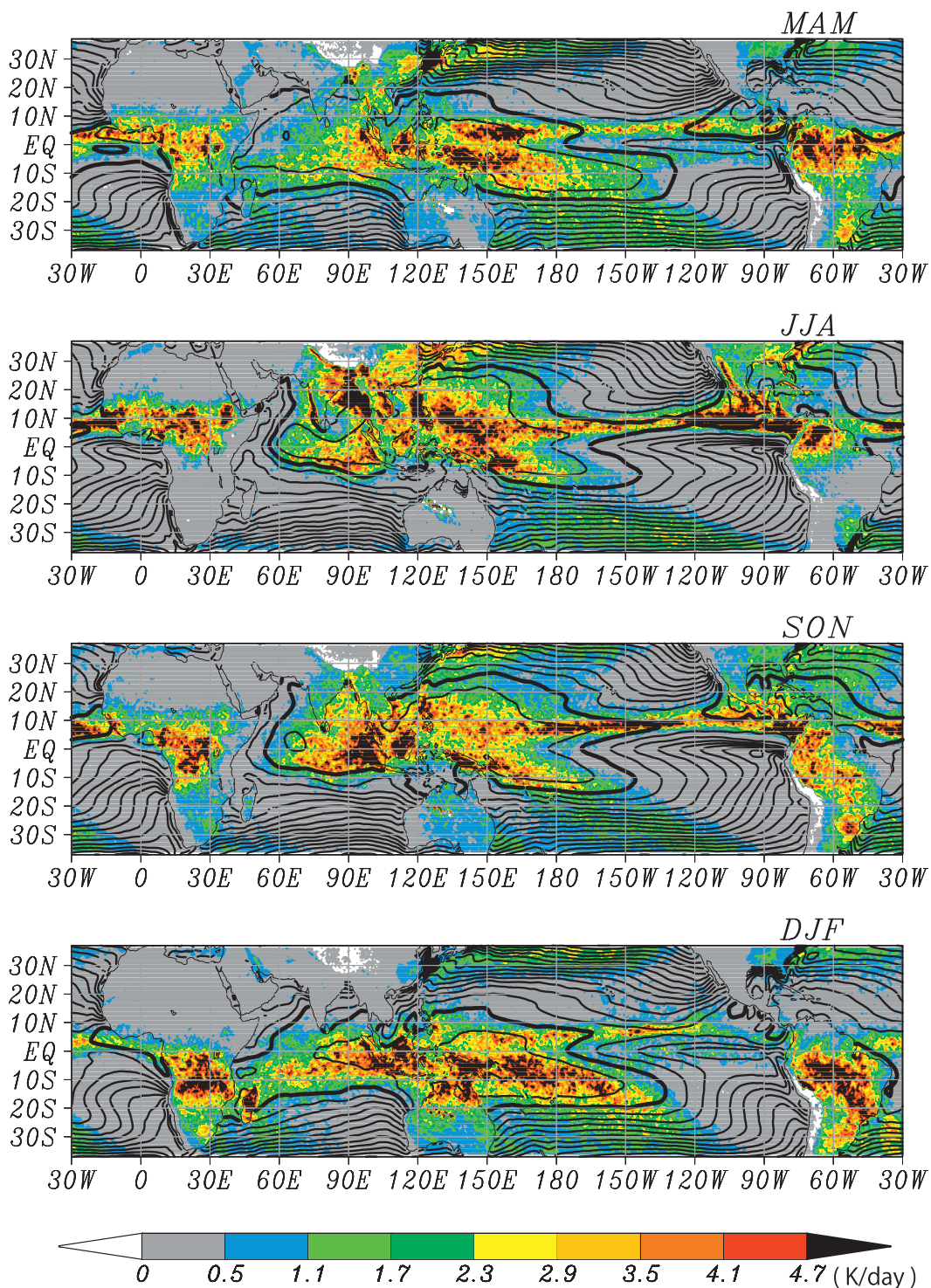
FIG. 2. The 8-yr unconditional mean $Q_1 - Q_R$ at 7.5 km for each season in color shades, with SST distribution in contours. Contour interval (CI) is 1.0°C and thick contours are for 28°C.
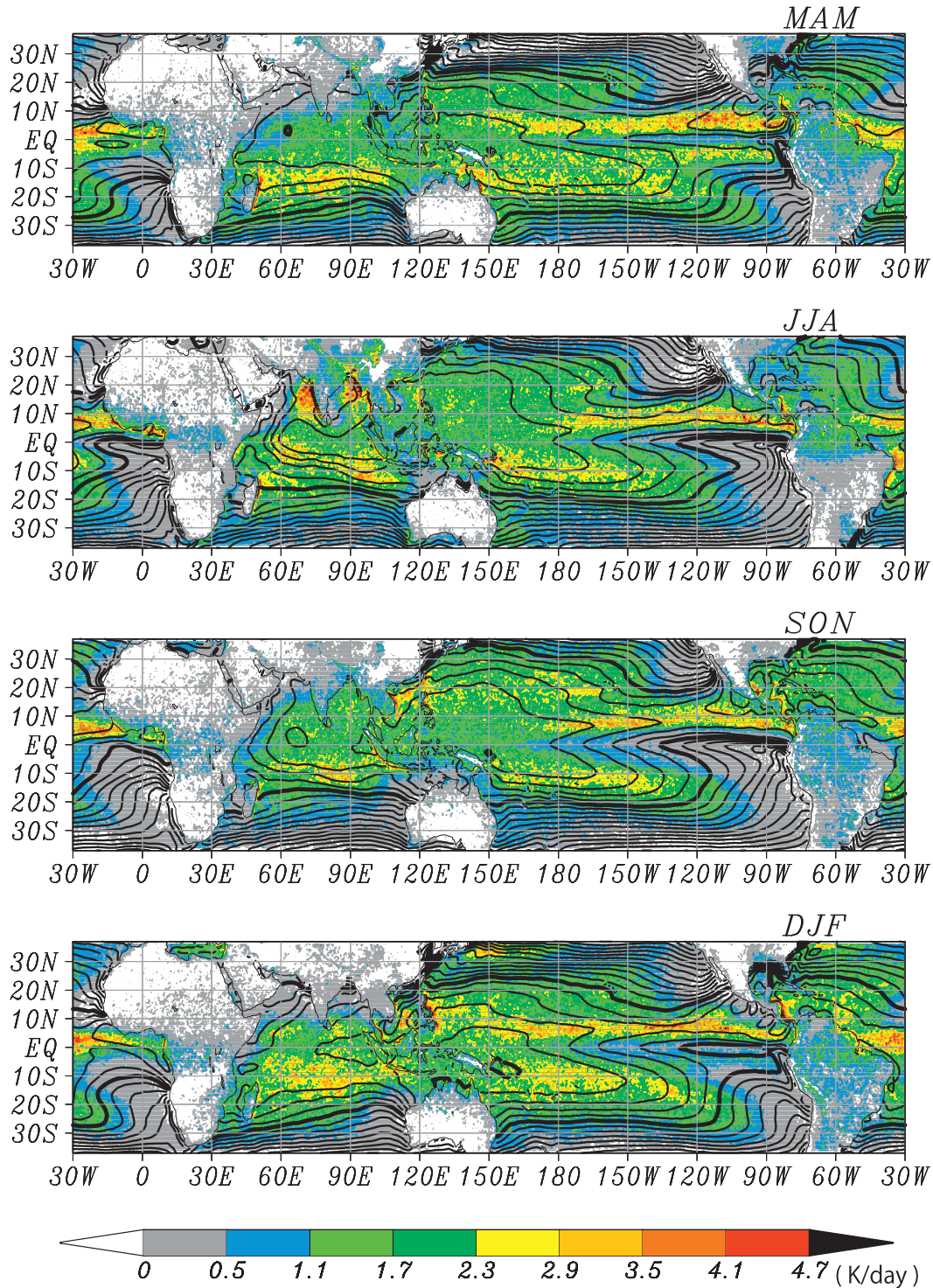
FIG. 3. As in Fig. 2, but for $Q_1 - Q_R$ at 2.0 km. Thick contours are for 25° and 30°C.

(e.g., Yuan et al. 2008), we next examine the scatter of $Q_1 - Q_R$ for deep heating and for shallow heating, against the pressure velocity ($dp/dt = \omega$) at 500 hPa ($\omega 500$) for the December–February season in Figs. 6 and 7, respec-

tively. Heating from the deep systems correlates much better (-0.85 to -0.87) with $\omega 500$ compared to that with SST. On the other hand, shallow congestus heating is not directly related to the effects of large-scale subsidence,
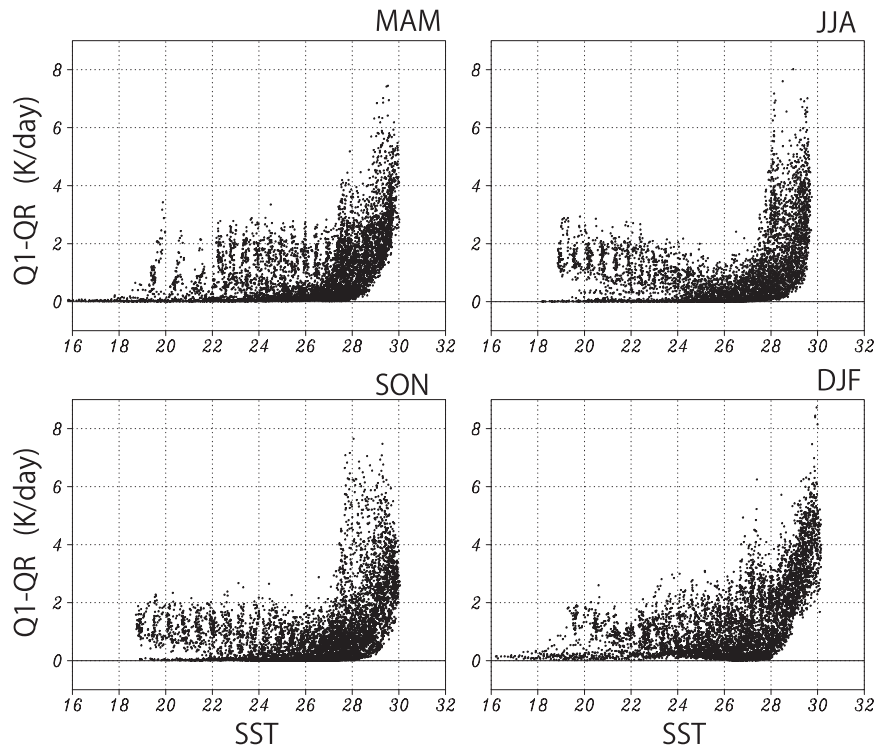
FIG. 4. Scatter diagrams of 8-yr unconditional mean $Q_1 - Q_R$ at 7.5 km against SST at the same $1° \times 1°$ grid for each season.

which is consistent with what was implied from the heating–SST relationship in Fig. 5. It is also interesting to find there is no significant seasonal dependency in these environment–heating relationships, either with SST or with large-scale subsidence (Figs. 4–7).

A longitude–height section of the 8-yr unconditional mean $Q_1 - Q_R$ along 10°S for the September–November season and the saturated equivalent potential temperature is plotted in Fig. 8. Over the western and central south Pacific from 150°E to 170°W, active deep heating is observed together with shallow heating. The eastern south Pacific from 160° to 80°W corresponds to the large-scale subsidence region under the influence of the subtropical high, and there is a stable layer just below 700 hPa. The convective heating is significantly suppressed at the height of the stable layer, suggesting the predominance of congestus heating. A similar structure is also found over the southeastern Atlantic and over the southwestern Indian Ocean. Note that, although the deep- and shallow-mode distinction corresponds to $\omega 500$ over the ocean, it is not the same for those over land. In the JRA data, deep heating is observed over land even without average upward velocity at the midtroposphere over the South America (~60°W). We also examined this point with the 40-yr European Centre for Medium-Range Weather Forecasts (ECMWF) Re-Analysis (ERA-40)

data (not shown), although midtropospheric vertical velocities with ERA-40 are not downward at deep-heating longitudes over the South America; however, they show very small upward velocities that are distinct from those over the ocean.

To examine the above west–east contrast in heating and environment more closely, unconditional average vertical profiles of the $Q_1 - Q_R$ for the southwestern Pacific (SWPac) region (13°–3°S, 155°–165°E) and for the southeastern Pacific (SEPac) region (15°–5°S, 155°–145°W) for the September–November season are compared in Fig. 9. Over the SWPac (Fig. 9a), deep convective heating at ~5 km is as large as 3.4 K day^{-1} and shallow heating is found at a slightly higher than tropical average altitude of ~2.2 km found in Fig. 1. The thermodynamic profile in this region is slightly conditionally unstable in the lower troposphere but almost neutral (Fig. 9c). On the other hand, deep systems are clearly suppressed in the SEPac (Fig. 9b). Thermodynamic profiles evidently indicate the subsidence with a stable layer in the lower troposphere between 700 and 850 hPa, which establishes a very dry environment in the lower half of the troposphere (Fig. 9d). It is evident that deep convection is effectively suppressed with this subsiding dry layer.

Mass-integrated $Q_1 - Q_R$ values are 198.0 J s^{-1} (6.85 mm day^{-1}) in the SWPac and 68.8 J s^{-1}
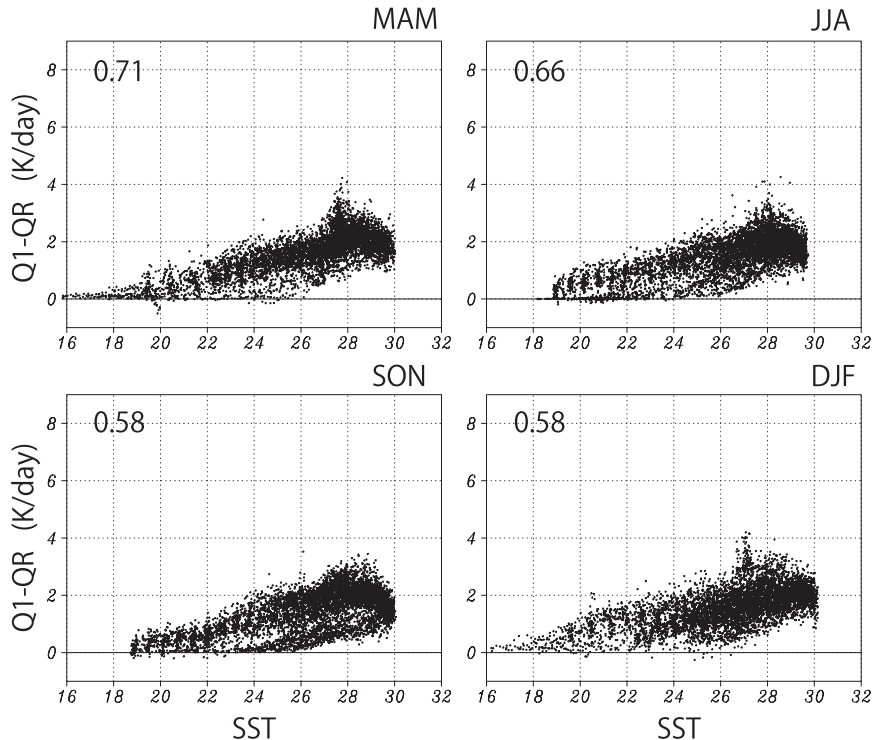
FIG. 5. As in Fig. 4, but for $Q_1 - Q_R$ at 2 km. Numbers at top left indicate correlation coefficients between SST and $Q_1 - Q_R$ at 2 km.

(2.38 mm day^{-1}) in the SEPac, respectively. It is notable that a substantial amount of rain, as large as 2.38 mm day^{-1} on average, comes from congestus rain under the large-scale subsiding circulation. The shallow-heating (<4.5 km) ratio to the total heating is 37.2% over the southwest Pacific region and 65.8% over the southeast Pacific region.

So far we have seen that shallow congestus heating is yielded by warm SSTs and that deep-system heating is well suppressed by the large-scale subsidence. To confirm if this discussion is applicable to the global tropics, we overlay the $\omega 500$ field onto the heating fields in Figs. 10a,b. It is evident that, while low-level congestus heating does not feel the effects of large-scale subsidence, deep-heating distribution clearly follows the zero contour of $\omega 500$, especially over the ocean. Figure 10c depicts the ratio of 2.0-km heating against the 7.5-km heating. In the subsidence region, the shallow heating is generally more than factor of 6 larger than the deep heating. For the large-scale vertical motion, we utilized the seasonal mean values of $\omega 500$. Midlevel subsidence does not always consist of compensating subsidence induced by deep convective activity but can be also dynamically induced over the subtropical highs (e.g., Miyasaka and Nakamura 2005). In other words, deep heating is interpreted to be "dynamically bounded" by the large-scale circulation.

To analyze the effect of vertical velocity on diabatic heating, we next stratify the conditional mean $Q_1 - Q_R$ profiles against $\omega 500$ for total, convective, and stratiform rain (Fig. 11). From heating profiles associated with total rain, we can find a clear bimodal structure, one with top-heavy heating associated with mesoscale convective systems with maximum between 6–8 km and another with shallow heating with a peak at around 2 km and a slight cooling just above. As already noted in the introduction,
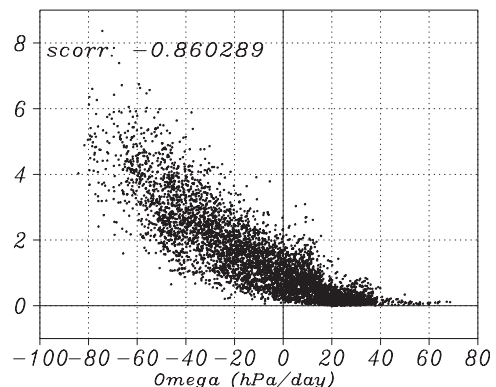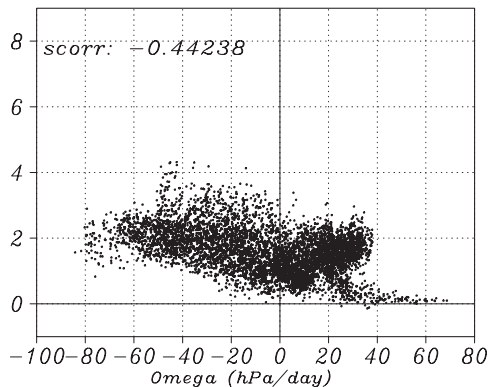

FIG. 6. Scatter diagram of 8-yr unconditional mean $Q_1 - Q_R$ at 7.5 km against dp/dt at 500 hPa at the same $1° \times 1°$ grid for the December–February season.

FIG. 7. As in Fig. 6, but for $Q_1 - Q_R$ at 2 km.

the bimodal structure focused on here consists of deep modes and congestus modes, excluding the shallow trade cumulus modes because of the sensitivity limit of TRMM PR. These two modes switch their dominance at around $\omega \sim 0$. When the heating is separated into convective and stratiform rain parts (Figs. 11b,c), it is noticed that convective rain is largely affected by the large-scale subsidence in a manner that deep heating at $\sim$5 km is significantly suppressed, whereas the stratiform rain is not directly affected but slightly lowers its height. This height shift is probably because of the lower

melting level height associated with lower SSTs in the subsidence region.

Figure 12 depicts the environmental profiles against ω500 for relative humidity (RH) and for saturated equivalent potential temperature θ_{se}, respectively, in the same manner as in Fig. 11. In the large-scale subsidence region, a very dry atmosphere with relative humidity less than 40% is found from 400 to 700 hPa. When the average subsidence is larger than 20 hPa day^{-1}, the RH is less than 30% between 500 and 700 hPa, which can strongly discourage the development of deep convection beyond the freezing level. As for the temperature profiles, lower-tropospheric conditional instability is concentrated in the ascending region for ω500 < -50 hPa day^{-1}. In the intermediate range of $-10 < \omega$500 < 40 hPa day^{-1}, there is a lower-level stable layer around 700 hPa. For ω500 > 40 hPa day^{-1}, the temperature profile is conditionally neutral.

Because large-scale vertical velocity and SST distributions are usually closely related to each other, it is difficult to separate effects of the former from the latter; therefore, we examine the effects of vertical velocity on the total $Q_1 - Q_R$ separately over limited SST grids of 22.0°–23.0°, 24.0°–25.0°, 26.0°–27.0°, and 28.0°–29.0°C, respectively (Fig. 13). In all cases, very similar bimodal structures of heating as we saw in Fig. 11a are found.
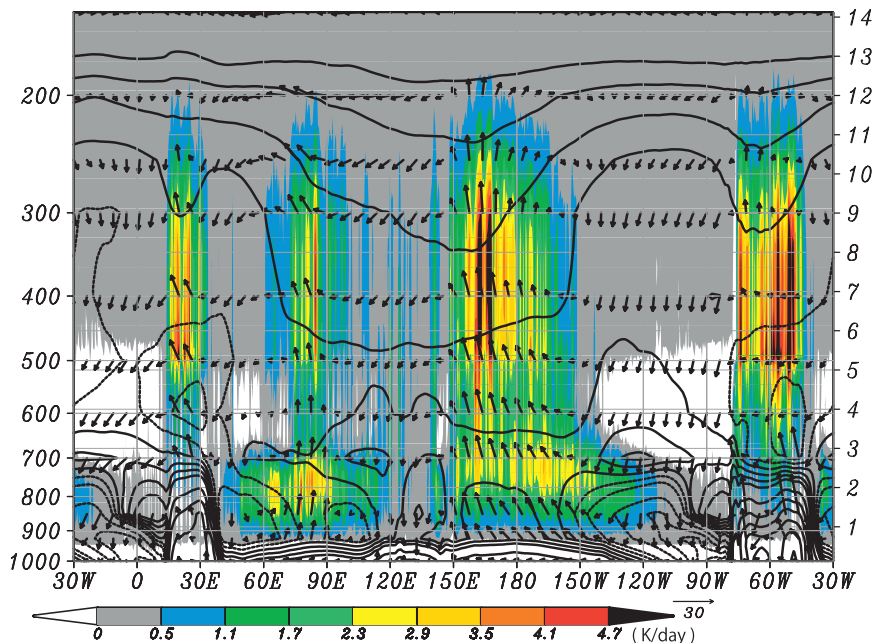

FIG. 8. Longitude–height section of 8-yr unconditional mean $Q_1 - Q_R$ at 10°S for September–November season (color shades) and the θ_{se} in contours (K). Contour levels are set at 320, 325, 330, 335, 340, 342, 344, 346, 348, 350, 355, 360, 365, and 370 K; values less than 344 K are contoured in dashed lines. Vectors indicate zonal and vertical wind velocity. The unit vector at the bottom indicates the scale of the zonal wind speed in m s^{-1} and the vertical velocity is stretched to appear clearly in the figure.
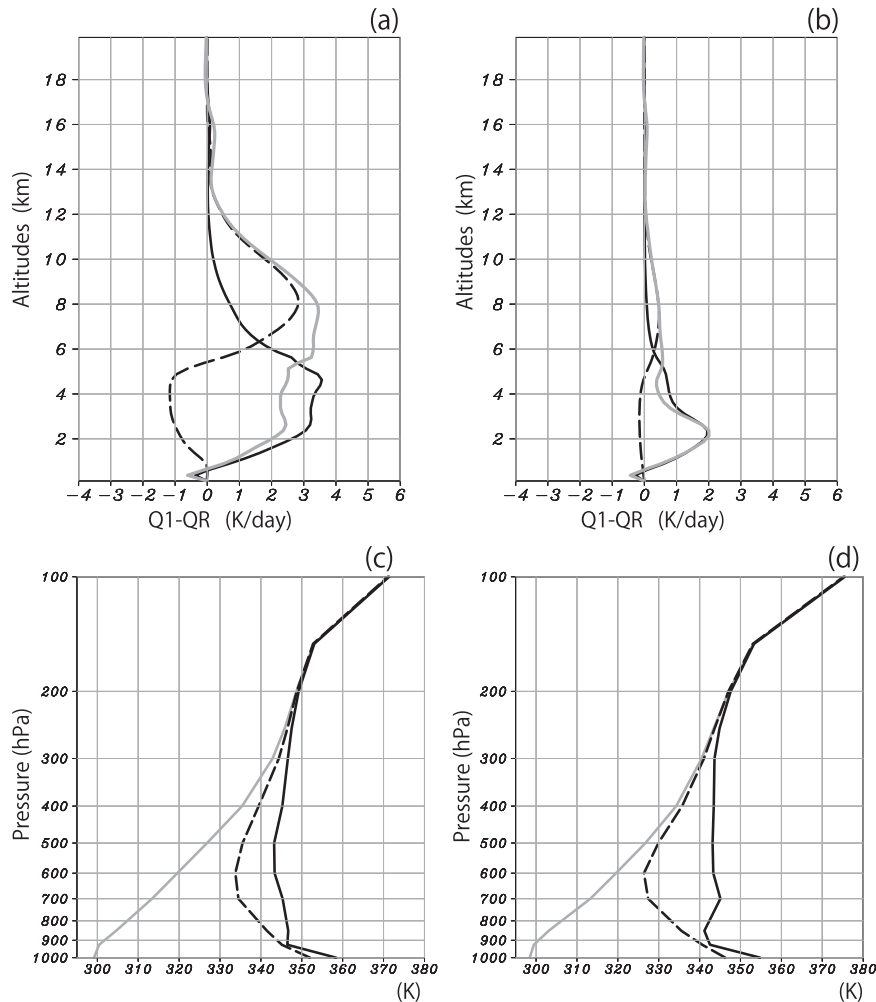
FIG. 9. Eight-year mean vertical profiles of the $Q_1 - Q_R$ averaged for the (a) SWPac and (b) SEPac regions, for the September–November season. Black solid lines represent $Q_1 - Q_R$ associated with convective rain, black-dashed lines represent $Q_1 - Q_R$ with stratiform rain, and gray lines are for total rain. (c),(d) As in (a),(b), respectively, but for potential temperature (K, gray solid lines), equivalent potential temperature (dashed lines), and θ_{se} (K, black solid lines).

Moreover, the transition region from the deep mode to the shallow mode is found very similarly around zero vertical velocity, although there is a slight shift toward the ascending regions as the SST increases. The suppression of the deep mode is significant even over very warm SSTs of 28.0°–29.0°C in the subsidence regions. The predominance of the deep mode with increasing upward vertical velocity is also apparent in all SST ranges. By examining the cloud radiative forcing as a function of $\omega500$, Yuan et al. (2008) found that the thick high cloud amount strongly increases with increasing upward vertical velocity and that such a relationship hardly changes even when cases are restricted to SST > 28°C. It is consistent with the increase of the deep mode in our analysis.

Figure 14 depicts RH profiles stratified against $\omega500$ for separate SST conditions. In all cases, basic dependency on $\omega500$ is fairly similar to Fig. 12a. Boundary layers are very humid over all velocity ranges, the upper troposphere is also humid in the large-scale ascending regions, and a significant mid–lower-tropospheric dry layer is found in the large-scale subsidence regions. The levels of all these structures shift upward as SST increases. The middle altitudes of the lower-tropospheric dry layer in the subsidence region are 600, 550, 500, and 400 hPa for SST = 22.0°–23.0°, 24.0°–25.0°, 26.0°–27.0°, and 28.0°–29.0°C, respectively. A very moist boundary layer also thickens as the SST increases, and the level of the upper-tropospheric moist layer in the ascending region also significantly increases and deepens.
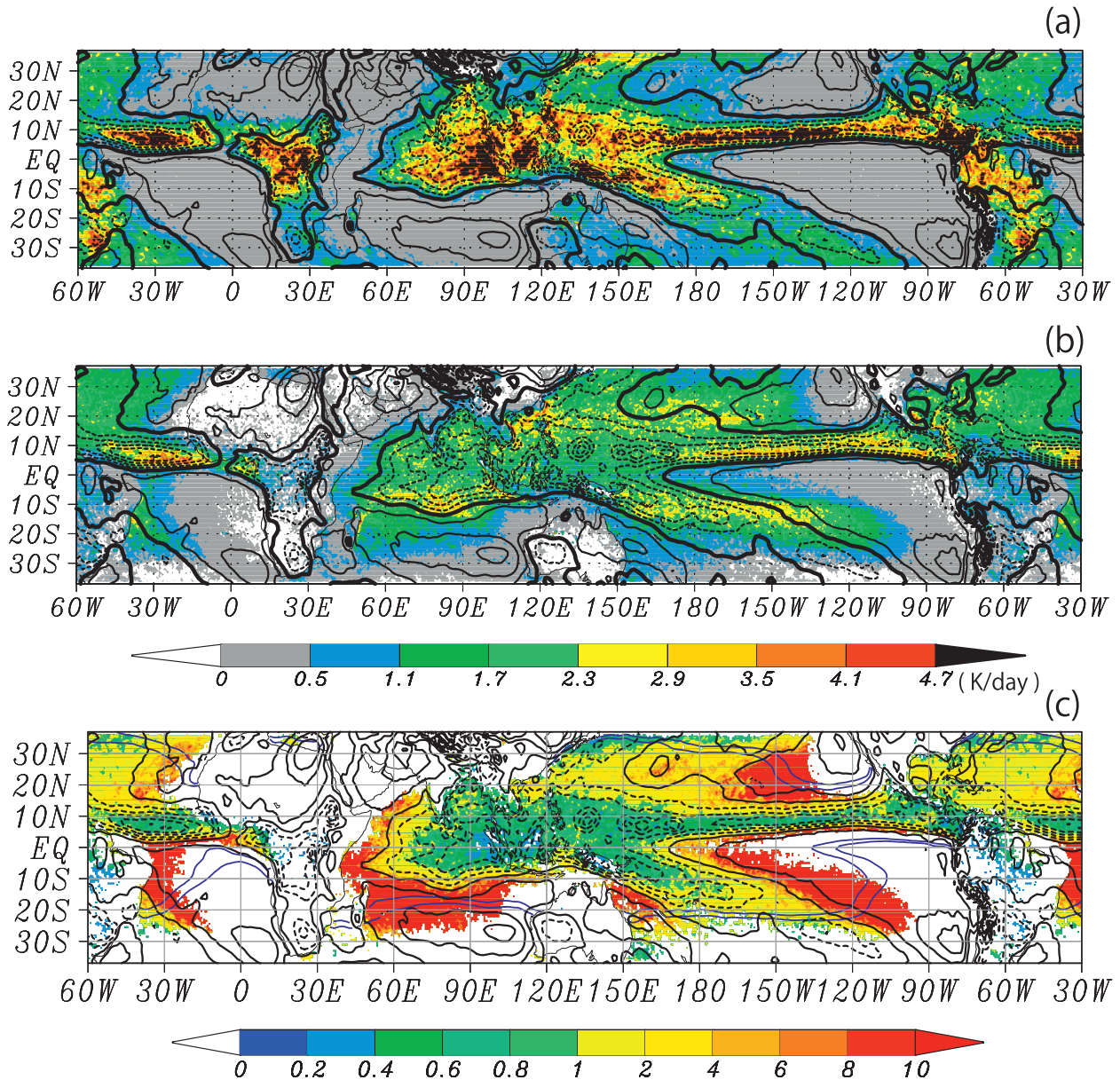
FIG. 10. The 8-yr unconditional mean $Q_1 - Q_R$ at (a) 7.5 and (b) 2.0 km and (c) their ratio (2.0 km/7.5 km) for the September–November season in color shade with dp/dt at 500 hPa in contours. CI 10 hPa day^{-1}, and negative values are indicated with dashed lines. Thick solid contours are for zero values.

In contrast, dependencies of thermodynamic profiles against $\omega 500$ in different SST ranges are different from the averaged feature seen in Fig. 12b (not shown); in each 2°C SST range, thermodynamic profiles do not vary largely with $\omega 500$, which means that atmospheric thermodynamic condition is largely determined by SST. It is realized that the average feature in Fig. 12b consists of combinations of these profiles.

In summary, a bimodal feature in the nondrizzle precipitation systems is found from the precipitation-associated latent heating over a wide range of SSTs. The transition from deep systems to cumulus congestus is basically independent of SST and controlled by the large-scale subsidence represented with the seasonal average $\omega 500$. The lower-tropospheric dry layer associated with large-scale subsidence is suggested to be the major environmental factor that suppresses deep convection.

5. Summary and discussion

In this study, we analyze three-dimensional distributions of $Q_1 - Q_R$ estimated from TRMM PR utilizing
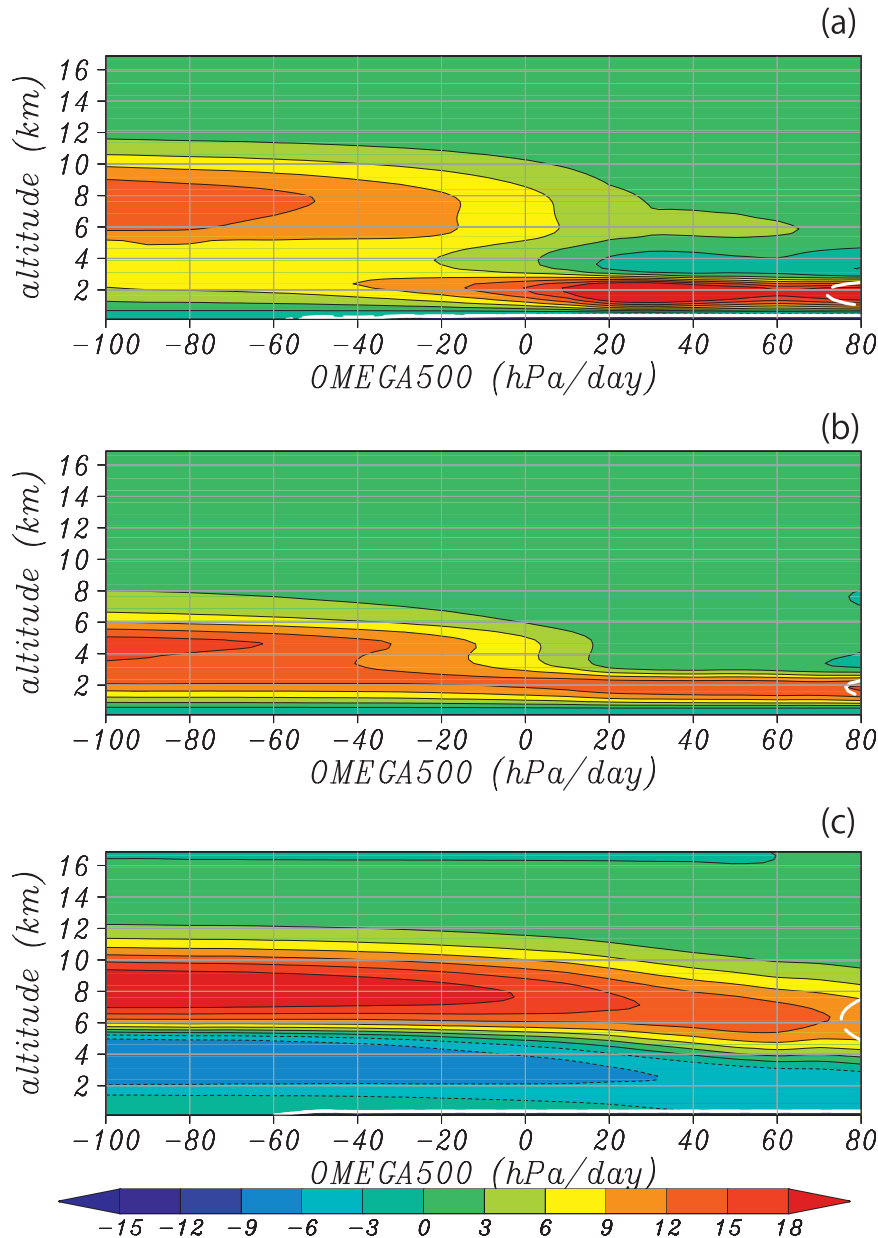
FIG. 11. The 7-yr conditional mean $Q_1 - Q_R$ profiles stratified with dp/dt at 500 hPa averaged for September–November season and for 30°N–30°S at all lons over the ocean, associated with (a) all rain, (b) convective rain, and (c) stratiform rain. Factors 10, 2.5, and 10 are multiplied to the values for color scale. White contours indicate the error bars for 3 and 6 in the same scale as the color shade.

the SLH algorithm. Mass-integrated $Q_1 - Q_R$ averaged over the ocean from 30°N to 30°S is estimated as ~72.6 J s^{-1} (~2.51 mm day^{-1}), and that averaged over land from 30°N to 30°S is ~73.7 J s^{-1} (~2.55 mm day^{-1}). It is shown that nondrizzle precipitation over tropical and subtropical oceans consists of two dominant modes of rainfall sytems: deep systems and congestus. A rough estimate of shallow-heating contribution against the total

heating is about 46.7% for the average tropical oceans from 30°N to 30°S, which is substantially larger than the 23.7% averaged over land for the same latitudes. A large contribution from congestus rain, particularly in the eastern Pacific ITCZ region, is consistent with recent studies that focus on the importance of the shallow mode in that region (Zhang et al. 2004; Kubar and Hartmann 2008).
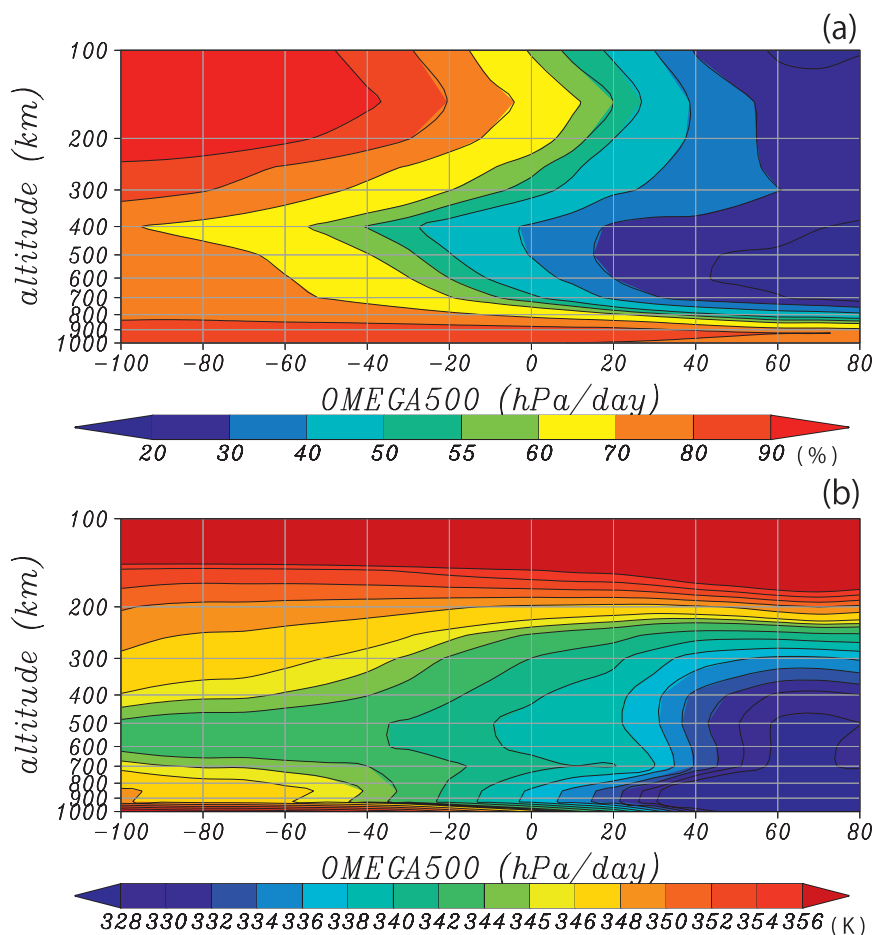
FIG. 12. As in Fig. 11, but for (a) RH and (b) θ_{se}.

Next, relationships of shallow- and deep-mode amplitudes to the environmental condition are examined. It is found that, although cumulus congestus linearly increases with SST, deep mode is effectively bounded by large-scale subsidence. A typical mass-integrated $Q_1 - Q_R$ value in the deep convective region in SWPac is 198.0 J s^{-1} (6.85 mm day^{-1}), and that in the congestus region in SEPac is 68.8 J s^{-1} (2.38 mm day^{-1}). It is notable that a substantial amount of rain, as large as 2.38 mm day^{-1} on average, is brought from congestus clouds under the large-scale subsiding circulation. The shallow-heating (<4.5 km) ratio to the total heating is 37.2% over SWPac, whereas it is 65.8% in SEPac. Thermodynamic effects and dynamical effects of the environment are separated by comparing the vertical velocity dependences in different SST ranges. It is found that, even in the region with SSTs warmer than 28°C, large-scale subsidence effectively suppresses deep convection, with congestus heating still remaining. This result strongly supports the hypothesis that the mid–lower-tropospheric dry layer, which accompanies the large-scale

subsidence, plays an essential role to suppress deep convection through entrainment as suggested by Raymond and Blyth (1992) and Blyth (1993).

Wu (2003) suggested that shallow heating induces surface circulation much more effectively than deep heating, thus resulting in larger low-level moisture convergence. Existence of a substantial amount of congestus heating may be essential to maintain deep systems. Khouider and Majda (2007) emphasized the importance of the existence of congestus cloud heating, in addition to deep convective heating and deep stratiform heating, in reproducing realistic convectively coupled equatorial wave modes. Because our results show that congestus heating substantially contributes to global tropical rain, it is essential to reproduce this amount of shallow rain to understand the global circulation correctly.

With various AGCMs, an unrealistic double-ITCZ problem is reported. Our results suggest that cumulus congestus certainly follows the lower-level destabilization with warm SST, but it is not the sufficient condition for deep systems to be generated. Deep systems are
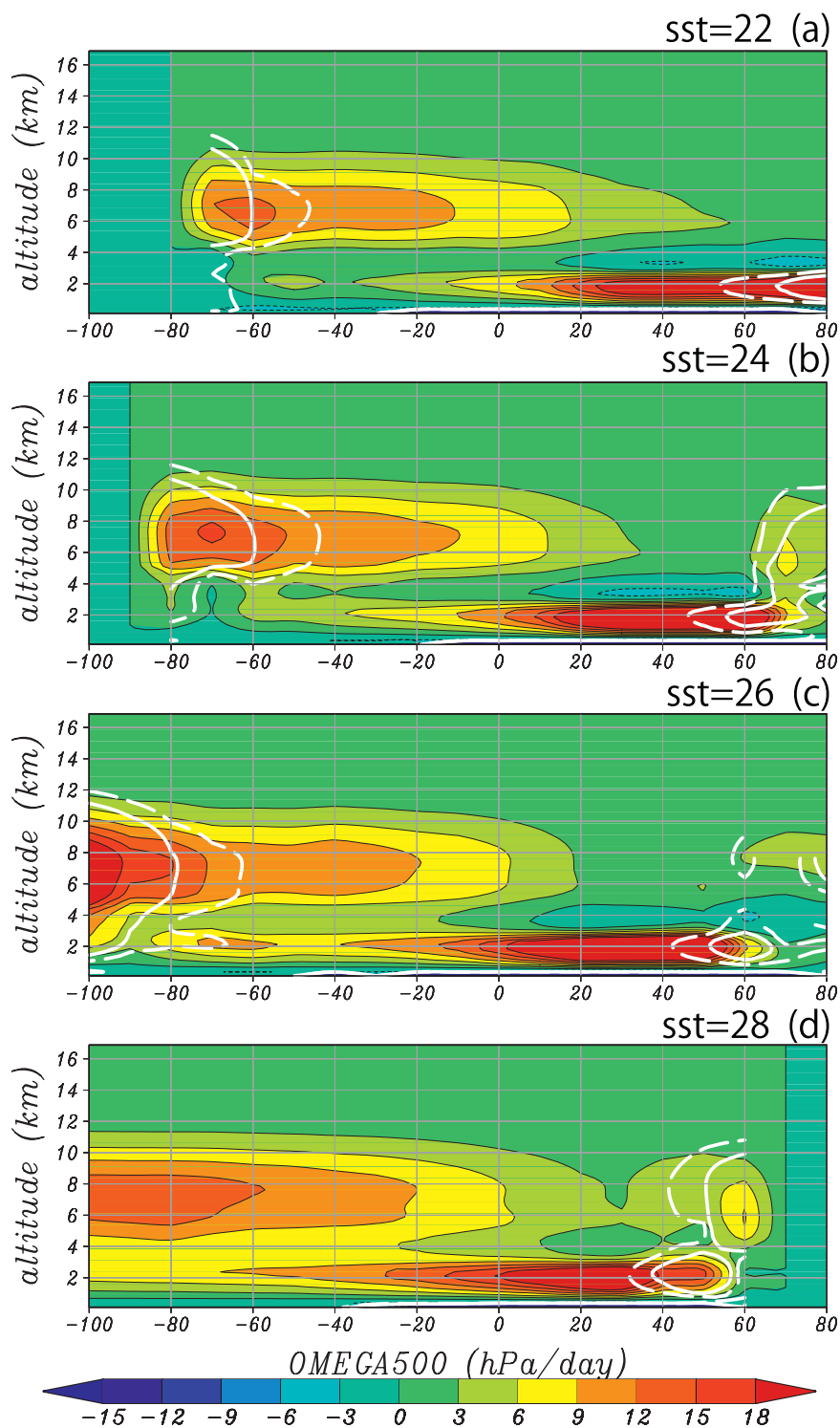
FIG. 13. As in Fig. 11, but for all rain averaged over the grids with SST of (a) 22.0°–23.0°, (b) 24.0°–25.0°, (c) 26.0°–27.0°, and (d) 28.0°–29.0°C. White contours depict where 99% significance level with the Student's *t* test attains 3.0 and 6.0 in the same scale as color shades.
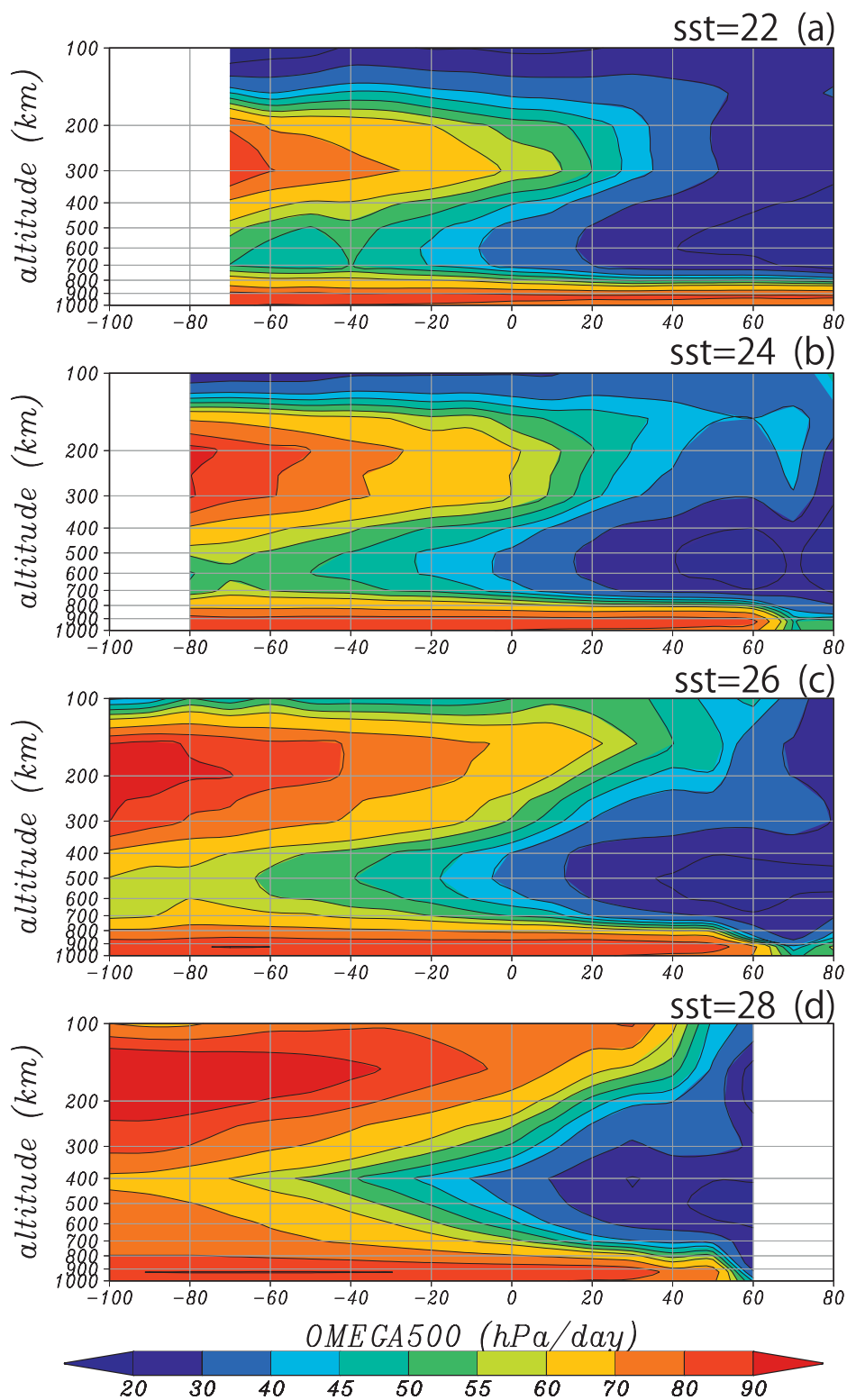
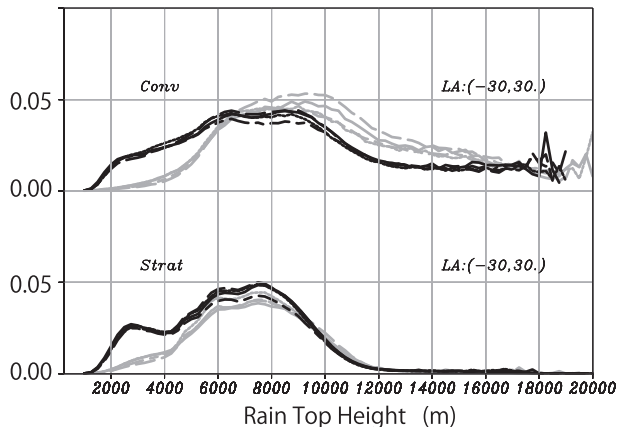FIG. 14. As in Fig. 13, but for vertical profiles of RH.

FIG. A1. Contribution to the surface rain from every 250-m RTH bin for (top) convective rain and (bottom) stratiform rain. Abscissa is RTH (m) and ordinate is rain contribution (mm day^{-1}), in the same manner as in Takayabu (2006). Black curves are for seasonal averages over the oceans from 30°N to 30°S at all lons and gray ones are those over land averaged for 1998–2000.

strictly bounded by large-scale subsidence. It is strongly suggested that a realistic parameterization that represents the suppression of deep systems by large-scale subsidence independent of SST is essential to overcome the double-ITCZ problem, as well as to generate realistic large-scale circulation. Because our results support that the entrainment of dry lower-tropospheric air is a major factor suppressing deep convection, representation of the realistic entrainment is very important.

APPENDIX

Rain-Top Height Statistics

With Fig. 1, we have discussed that cumulus congestus heating is significant over ocean but not over land. Here, we want to see this point again by examining contributions to the surface rain from each 250-m bin of rain-top height (RTH) in the same manner as in Takayabu (2006;

Fig. A1), based on TRMM PR data. We can find that a significant convective rain over the ocean starts from altitudes of 2–6 km, which is absent over land. On the other hand, contributions to the convective rain from 8 to 16-km RTH are much higher over land than over the ocean. We identify the former relatively shallower RTH contributions with the ~2-km-height heating peak and call it congestus heating. Note that, as for RTHs of deep stratiform rain, large contributions are found at altitudes from 6–8 km and there is not much difference found between over the ocean and over land. There is a difference in relatively shallow stratiform rain with RTHs of 2–3 km, which is significant only over the ocean. However, note that, because shallow rain does not accompany the bright band, it is difficult to distinctly separate the shallow stratiform rain from the shallow convective rain.

REFERENCES

Back, L. E., and C. S. Bretherton, 2009: A simple model of climatological rainfall and vertical motion patterns over the tropical oceans. *J. Climate,* **22,** 6477–6497.
Blyth, A. M., 1993: Entrainment in cumulus clouds. *J. Appl. Meteor.,* **32,** 626–641.
Bony, S., and J.-L. Dufrence, 2005: Marine boundary layer clouds at the heart of tropical cloud feedback uncertainties in climate models. *Geophys. Res. Lett.,* **32,** L20806, doi:10.1029/2005GL023851.
Brown, R. G., and C. Zhang, 1997: Variability of midtropospheric moisture and its effect on cloud-top height distribution during TOGA COARE. *J. Atmos. Sci.,* **54,** 2760–2774.
Gadgil, S., P. V. Joseph, and N. V. Joshi, 1984: Ocean–atmosphere coupling over monsoon regions. *Nature,* **312,** 141–143.
Houze, R. A., 1993: *Cloud Dynamics.* Academic Press, 573 pp.
Jensen, M. P., and A. D. Del Genio, 2006: Factors limiting convective cloud-top height at the ARM Nauru Island climate research facility. *J. Climate,* **19,** 2105–2117.
Johnson, R. H., T. M. Rickenbach, S. A. Rutledge, P. E. Ciesielski, and W. H. Schubert, 1999: Trimodal characteristics of tropical convection. *J. Climate,* **12,** 2397–2418.
Khouider, B., and A. J. Majda, 2007: A simple multicloud parameterization for convectively coupled tropical waves. Part II: Nonlinear simulations. *J. Atmos. Sci.,* **64,** 381–400.
Kikuchi, K., and Y. N. Takayabu, 2004: The development of organized convection associated with the MJO during TOGA COARE IOP: Trimodal characteristics. *Geophys. Res. Lett.,* **31,** L10101, doi:10.1029/2004GL019601.
Kubar, T. L., and D. L. Hartmann, 2008: Vertical structure of tropical oceanic convective clouds and its relation to precipitation. *Geophys. Res. Lett.,* **35,** L03804, doi:10.1029/2007GL032811.
Mapes, B. E., 2000: Convective inhibition, subgrid-scale triggering energy, and stratiform instability in a toy tropical wave model. *J. Atmos. Sci.,* **57,** 1515–1535.
Miyasaka, T., and H. Nakamura, 2005: Structure and formation mechanisms of northern summertime subtropical highs. *J. Climate,* **18,** 5046–5065.
Petty, G. W., 1999: Prevalence of precipitation from warm-topped clouds over eastern Asia and the western Pacific. *J. Climate,* **12,** 220–229.

Raymond, D. J., and A. M. Blyth, 1992: Extension of the stochastic mixing model to cumulonimbus clouds. *J. Atmos. Sci.,* **49,** 1968–1983.

Redelsperger, J.-L., D. B. Parsons, and F. Guichard, 2002: Recovery processes and factors limiting cloud-top height following the arrival of a dry intrusion observed during TOGA COARE. *J. Atmos. Sci.,* **59,** 2438–2457.

Schumacher, C., M. H. Zhang, and P. E. Ciesielski, 2007: Heating structures of the TRMM field campaigns. *J. Atmos. Sci.,* **64,** 2593–2610.

——, P. E. Ciesielski, and M. H. Zhang, 2008: Tropical cloud heating profiles: Analysis from KWAJEX. *Mon. Wea. Rev.,* **136,** 4289–4300.

Shige, S., Y. N. Takayabu, W.-K. Tao, and D. E. Johnson, 2004: Spectral retrieval of latent-heating profiles from TRMM PR data. Part 1: Development of a model-based algorithm. *J. Appl. Meteor.,* **43,** 1095–1113.

——, ——, ——, and C.-L. Shie, 2007: Spectral retrieval of latent heating profiles from TRMM PR data. Part II: Algorithm improvement and heating estimates over tropical ocean regions. *J. Appl. Meteor. Climatol.,* **46,** 1098–1124.

——, ——, and ——, 2008: Spectral retrieval of latent heating profiles from TRMM PR data. Part III: Estimating apparent moisture sink profiles over tropical oceans. *J. Appl. Meteor. Climatol.,* **47,** 620–640.

Short, D. A., and K. Nakamura, 2000: TRMM radar observations of shallow precipitation over tropical oceans. *J. Climate,* **13,** 4107–4124.

Takayabu, Y. N., 2006: Rain-yield per flash calculated from TRMM PR and LIS data and its relationship to the contribution of tall convective rain. *Geophys. Res. Lett.,* **33,** L18705, doi:10.1029/2006GL027531.

——, J. Yokomori, and K. Yoneyama, 2006: A diagnostic study on interactions between atmospheric thermodynamic structure and cumulus convection over the tropical western Pacific Ocean and over the Indochina Peninsula. *J. Meteor. Soc. Japan,* **84A,** 151–169.

Takemi, T., O. Hirayama, and C. Liu, 2004: Factors responsible for the vertical development of tropical oceanic cumulus convection. *Geophys. Res. Lett.,* **31,** L11109, doi:10.1029/2004GL020225.

Wu, Z., 2003: A shallow CISK, deep equilibrium mechanism for the interaction between large-scale convection and large-scale circulation in the tropics. *J. Atmos. Sci.,* **60,** 377–392.

Yanai, M., S. Esbensen, and J.-H. Chu, 1973: Determination of bulk properties of tropical cloud clusters from large-scale heat and moisture budgets. *J. Atmos. Sci.,* **30,** 611–627.

Yokoyama, C., and Y. N. Takayabu, 2008: A statistical study on rain characteristics of tropical cyclones using TRMM satellite data. *Mon. Wea. Rev.,* **136,** 3848–3862.

Yuan, J., D. L. Hartmann, and R. Wood, 2008: Dynamic effects on the tropical cloud radiative forcing and radiation budget. *J. Climate,* **21,** 2337–2351.

Zhang, C., M. McGauley, and N. A. Bond, 2004: Shallow meridional circulation in the tropical eastern Pacific. *J. Climate,* **17,** 133–139.